



The AFRL Additive Manufacturing Modeling Challenge: Predicting Micromechanical Fields in AM IN625 Using an FFT-Based Method with Direct Input from a 3D Microstructural Image

Carter K. Cocke¹ · Anthony D. Rollett² · Ricardo A. Lebensohn³ · Ashley D. Spear¹

Received: 4 March 2021 / Accepted: 22 April 2021 / Published online: 17 May 2021
© The Minerals, Metals & Materials Society 2021

Abstract

The efficacy of an elasto-viscoplastic fast Fourier transform (EVPFFT) code was assessed based on blind predictions of micromechanical fields in a sample of Inconel 625 produced with additive manufacturing (AM) and experimentally characterized with high-energy X-ray diffraction microscopy during an in situ tensile test. The blind predictions were made in the context of Challenge 4 in the AFRL AM Modeling Challenge Series, which required predictions of grain-averaged elastic strain tensors for 28 unique target (Challenge) grains at six target stress states given a 3D microstructural image, initial elastic strains of Challenge grains, and macroscopic stress–strain response. Among all submissions, the EVPFFT-based submission presented in this work achieved the lowest total error in comparison with experimental results and received the award for Top Performer. A post-Challenge investigation by the authors revealed that predictions could be further improved, by over 25% compared to the Challenge-submission model, through several model modifications that required no additional information beyond what was initially provided for the Challenge. These modifications included a material parameter optimization scheme to improve model bias and the incorporation of the initial strain field through both superposition and eigenstrain methods. For the first time with respect to EVPFFT modeling, an ellipsoidal-grain-shape Eshelby approximation was tested and shown to improve predictive capability compared to previously used spherical-grain-shape assumptions. Lessons learned for predicting full-field micromechanical response using the EVPFFT modeling method are discussed.

Keywords Polycrystal plasticity · EVPFFT modeling · Residual strains · AFRL Challenge · Synchrotron X-rays · Microstructure

Introduction

The advent of metal additive manufacturing (AM) and its potential as a candidate replacement for conventional manufacturing in certain structural applications has created a need to advance predictive models that can support design and qualification practices. Developing such predictive models

is particularly challenging due to the complex physics underpinning process-structure-property relationships in metal AM, which has been highlighted in multiple recent review articles (e.g., [1–4]). While significant progress has been made in physics-based modeling of metal AM, there remains a lack of benchmarked, pedigreed measurements available to the community to assess model performance.

To help address this problem, the US Air Force Research Laboratory (AFRL) Materials & Manufacturing Directorate Structural Materials, Metals Branch (AFRL/RXCM) and America Makes launched the Additive Manufacturing (AM) Modeling Challenge Series in 2019. The Series was comprised of four distinct challenge problems that each served as a round-robin exercise designed to assess computational approaches for predicting process-structure or structure-property linkages at either macro- or microscales

✉ Ashley D. Spear
ashley.spear@utah.edu

¹ Department of Mechanical Engineering, University of Utah, Salt Lake City, UT, USA

² Department of Materials Science and Engineering, Carnegie Mellon University, Pittsburgh, PA, USA

³ Theoretical Division, Los Alamos National Laboratory, Los Alamos, NM, USA

in the context of metal AM. In general, time-constrained round-robin exercises, like the well-established Sandia Fracture Challenge [5–7] and the recently launched AM-Bench [8], play a critical role in advancing both state of the art and state of practice by identifying gaps in modeling techniques and assessing the relative importance of specific modeling assumptions on predictions of interest to the scientific and engineering communities. While AM-Bench [8] was the first modeling challenge in the relatively new arena of metal AM, its primary focus was on assessing process modeling to predict residual strain field, part distortion, and as-built microstructure. The AFRL AM Modeling Challenge Series is the first round-robin exercise to assess model predictions of mechanical properties in metal AM.

Challenge Problem 4 in the AFRL AM Modeling Challenge Series was the first challenge of its kind to solicit blind predictions of micromechanical response given an explicit 3D representation of an additively manufactured microstructure, which had been characterized using high-energy X-ray diffraction microscopy [9–12]. As noted by many authors, predicting micromechanical response is generally very successful when distributions are compared between experiments and simulations at the polycrystal (aggregate) level, e.g., texture prediction [13]. At the grain scale and finer, however, experiments show substantially more scatter than simulations [14, 15]. The difficulty in predicting micromechanical response at these lower length scales arises from the strong anisotropy of both elastic and plastic deformation of metals and the complex interactions between grains, as each individual orientation has to both deform according to its local constitutive properties but also accommodate its neighbors. This difficulty is exacerbated in metal AM because, unlike conventional manufacturing routes, the thermal gradients and rapid solidification that occur during the AM process—especially during laser-based AM—tend to result in higher residual strains, more “exotic” grain structures, and unique defect structures (including voids).

The aim of this work is (1) to predict grain-scale micromechanical response of an AM Inconel 625 (IN625) sample in the context of Challenge Problem 4 in the AFRL AM Modeling Challenge by using an elasto-viscoplastic fast Fourier transform (EVPFFT) code, and (2) to assess potential approaches for improving upon the Challenge-submission model by optimizing constitutive parameters and incorporating residual strains using various approaches. Among all submissions to Challenge Problem 4, the submission presented in this work achieved the lowest total error in comparison with experimental results and received the award for Top Performer. Through post-Challenge investigation, we show that—using no more information than what was originally provided to all participants—significant improvements can be achieved relative to the Challenge-submission model by optimizing constitutive parameters and incorporating

initial elastic strains provided for a set of Challenge grains. Key takeaways are offered for using EVPFFT modeling to predict micromechanical response given a 3D microstructural image and known initial elastic strains for a subset of grains in a microstructural volume.

Background: Challenge Overview

The goal of Challenge 4 in the AFRL AM Modeling Challenge series was to assess the performance of 3D micromechanical modeling approaches through blind predictions of grain-scale response in an experimentally characterized additively manufactured tensile test specimen. Predictions were required for 28 unique *Challenge grains* contained within the specimen. The specimen was initially built as a $5 \times 35 \times 5$ mm³ column from IN625 powder using laser powder bed fusion in an EOS M280 system with the build direction along the (loading) *y*-axis. The specimen then went through a stress relief heat treatment, hot isostatic pressing (HIP) to remove pores, and subsequent heat treatment. The specimen was then machined using wire electrical discharge machining (EDM) to reach the final tensile test geometry depicted in Fig. 1.

The tensile specimen was experimentally characterized during interrupted in-situ displacement-controlled loading up to 1% tensile strain in the RAMS3 load frame [16] at the Advanced Photon Source (APS) 1-ID-E beamline at Argonne National Laboratory. Three synchrotron X-ray techniques were utilized during testing. Micro-computed tomography (CT) was used to determine void structure and to assist with data registration. Near-field high-energy X-ray diffraction microscopy (nf-HEDM) was used to map 3D grain structure, including crystal orientations, at the initial unloaded state (S0), and far-field (ff) HEDM was used to measure the grain-averaged elastic strain tensors throughout the microstructure at S0 and at six subsequent stress states (S1–S6). During testing, the sample was loaded to each target stress state and held for several hours for ff-HEDM data collection. For measurements taken in the plastic regime, the sample was unloaded by approximately 50 MPa to avoid creep during the hold period. The CT and HEDM data were then merged to create a 3D reconstruction of the sample. The reconstructed dataset contained 29,663 unique features/grains with a mean equivalent sphere diameter (ESD) of 10.8 μm based on our analysis. For complete details regarding the experimental procedure, the reader is referred to the lead Challenge 4 overview articles by Menasche et al. [17] and Chapman et al. [18].

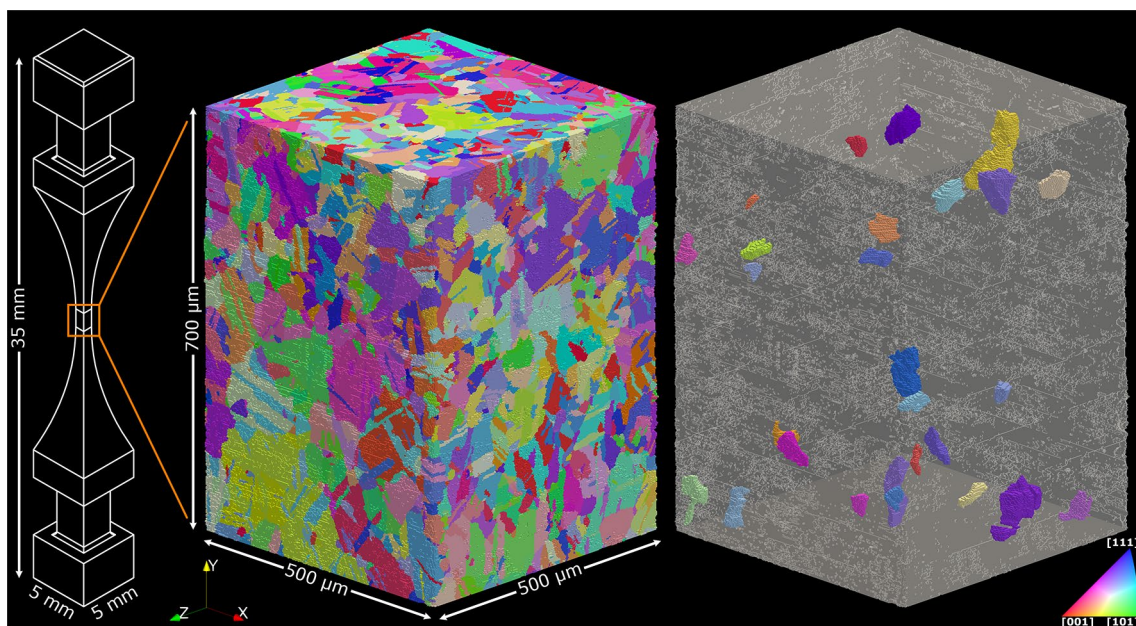


Fig. 1 Tensile specimen configuration and microstructural volume of interest for challenge 4 of the AFRL AM modeling series. The crystal orientations were characterized with nf-HEDM and are shown with

inverse pole figure (IPF) coloring. The 28 individual challenge grains are isolated at right

Experimental Data Provided to Participants

The dataset provided for the Challenge was given as a DREAM.3D [19] file containing feature (grain) data, voxel data, and crystal lattice information. The feature data provided for each grain included the average crystallographic orientation given as Bunge-Euler angles, the material phase, a Challenge grain indicator, and the initial grain-averaged elastic strain tensors. The initial elastic strain state was only provided for the 28 Challenge grains. The dataset included an outer border of “buffer zone” (air) to entirely contain sample surface roughness and fiducial markers. The 3D image (including both microstructure and buffer zone) was composed of perfectly cubic voxels with a 2 μm edge length and had $x \times y \times z$ dimensions of $305 \times 351 \times 312$ voxels ($610 \times 702 \times 624 \mu\text{m}^3$). The physical dimensions of the material microstructure absent the buffer zone were approximately $500 \times 700 \times 500 \mu\text{m}^3$. Figure 1 shows the 3D microstructure image and contained Challenge grains along with the tensile specimen geometry.

In addition to the microstructure data, AFRL provided participants with the aggregate engineering stress–strain curve for the tensile specimen, which was collected using the RAMS3 load frame to calculate engineering stress and two-point digital image correlation (DIC) measurement along the gauge region (a region larger than the characterized volume) to calculate the engineering strain. This experimental macroscopic response is shown in Fig. 2 with indicators for the target stress states at which the sample was held fixed and the

material was characterized using ff-HEDM. The provided macroscopic stress–strain curve was used for calibrating the constitutive model parameters, as described in Sect. 2.

Additional data were provided that were not used in this work. The additional data included tensile test data for

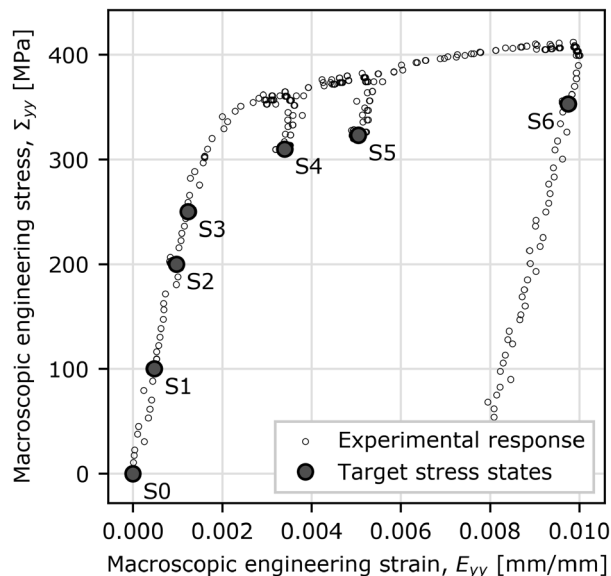


Fig. 2 Experimental macroscopic engineering stress–strain response from the in situ tensile test. The initial state (S0) and six target stress states (S1–S6) at which the sample was held for ff-HEDM data collection are indicated

auxiliary calibration samples tested at room and elevated temperatures and example images from post-mortem serial sectioning with electron backscatter diffraction (EBSD), backscattered electrons (BSE), and optical microscopy (OM). The phase fraction of observed precipitates was provided (1.2% volume fraction); however, the precipitates were not represented in the 3D microstructure image described above. For a complete description of all data provided to Challenge participants, please see the Challenge 4 overview articles by Menasche *et al.* [17] and Chapman *et al.* [18].

Quantities of Interest

Challenge participants were required to predict the six unique components of grain-averaged elastic strain tensors from the 28 unique Challenge grains at the six different target stress states (Fig. 2) for a total of 1008 predicted values. The 28 Challenge grains were chosen such that they were identified by ff-HEDM with high confidence at all six loading states, were entirely contained within the far-field sectioning region, and were uniquely correlated with grains from the nf-HEDM and EBSD serial sectioning. These 28 Challenge grains had dissimilar crystal orientations and spatial positions and can be seen in Fig. 1. Based on our analysis, the Challenge grains had a mean ESD of 32.2 μm , which was 197% larger than the mean ESD of all grains in the microstructure.

Performance Metrics

The Challenge was graded based on a summation of L2-norm errors for all 28 Challenge grains at all six target stress states. This grading metric corresponds to the following equation:

$$L2 = \sum_{S=1}^6 \sum_{g=1}^{28} \sqrt{\left(\epsilon_k^{e,\text{pred}} - \epsilon_k^{e,\text{exp}}\right)^2}, \quad (1)$$

where $\epsilon_k^{e,\text{pred}}$ and $\epsilon_k^{e,\text{exp}}$ are, respectively, the predicted and measured elastic strains of grain g at target stress state S written in contracted Voigt notation ($k = 1, 6$) to avoid double counting the symmetric shear strains.

Methods

EVPFFT Formulation

To make blind predictions for the AFRL Challenge, the elasto-viscoplastic fast Fourier transform (EVPFFT) modeling method was used. For an in-depth overview of this and other spectral modeling methods, see a recent review article by Lebensohn and Rollett [20]. The EVPFFT method

solves for micromechanical fields in a 3D Cartesian grid while fulfilling stress equilibrium and strain compatibility governing equations. A 3D microstructure image composed of cubic or cuboidal voxels (e.g., Fig. 1) can be defined as a unit cell discretized into a regular grid of points in Cartesian space, $\{\mathbf{x}\}$, and a corresponding grid of frequencies in Fourier space, $\{\boldsymbol{\xi}\}$, of the same dimensions. In this unit cell, the local strain field $\epsilon_{ij}(\mathbf{x})$ can be defined as an applied macroscopic strain E_{ij} plus a fluctuation (indicated by “~”) strain field as follows:

$$\epsilon_{ij}(\mathbf{x}) = E_{ij} + \tilde{\epsilon}_{ij}(\mathbf{x}). \quad (2)$$

This strain field is then solved alongside a thermo-elasto-viscoplastic constitutive equation [21] based on Hooke’s law, thermal strains (eigenstrains), dislocation-mediated mechanisms for single-crystal elasticity and plasticity, and Euler implicit time discretization, defined by the following:

$$\begin{aligned} \sigma_{ij}(\mathbf{x}) &= C_{ijkl}(\mathbf{x})\epsilon_{kl}^e(\mathbf{x}) \\ &= C_{ijkl}(\mathbf{x})\left(\epsilon_{kl}(\mathbf{x}) \right. \\ &\quad \left. - \epsilon_{kl}^*(\mathbf{x}) - \epsilon_{kl}^{p,t}(\mathbf{x}) - \dot{\epsilon}_{kl}^p(\mathbf{x}, \sigma)\Delta t\right), \end{aligned} \quad (3)$$

where $\sigma_{ij}(\mathbf{x})$ is the Cauchy stress tensor at time $t + \Delta t$; $C_{ijkl}(\mathbf{x})$ is the elastic stiffness tensor; $\epsilon_{kl}(\mathbf{x})$, $\epsilon_{kl}^*(\mathbf{x})$, and $\epsilon_{kl}^e(\mathbf{x})$ are, respectively, the total, thermal, and elastic strain tensors (at time $t + \Delta t$); $\epsilon_{kl}^{p,t}(\mathbf{x})$ is the plastic strain tensor (at time t); and $\dot{\epsilon}_{kl}^p(\mathbf{x})$ is the plastic strain-rate tensor given by:

$$\begin{aligned} \dot{\epsilon}_{ij}^p(\mathbf{x}, \sigma) &= \dot{\gamma}_0 \sum_{s=1}^{N_s} m_{ij}^s(\mathbf{x}) \left(\frac{|m_{kl}^s(\mathbf{x})\sigma_{kl}(\mathbf{x})|}{\tau^s(\mathbf{x})} \right)^n \\ &\quad \times \text{sgn}\left(m_{kl}^s(\mathbf{x})\sigma_{kl}(\mathbf{x})\right), \end{aligned} \quad (4)$$

where $\dot{\gamma}_0$ is the reference shear rate, N_s is the total number of slip systems, τ^s is the critical resolved shear stress (CRSS) of slip system s , n is the rate sensitivity exponent, and $m_{ij}^s = \frac{1}{2}(n_i^s b_j^s + n_j^s b_i^s)$ is the symmetric Schmid tensor of associated slip system s , with unit vectors n_i^s and b_i^s being the normal and Burgers vector directions of slip system s , respectively. For numerical convenience, $\dot{\gamma}_0 = 1$ and $n = 10$ as the Challenge did not include rate-sensitive effects; therefore, none were considered in our simulations. This leads to the expression involving the exponent n in Eq. (4) to be a convenient continuum approximation of Schmid’s law. The use of Eq. (3) with the addition of an eigenstrain field $\epsilon_{ij}^*(\mathbf{x})$ was first proposed by Pokharel and Lebensohn [21] as a generalization of the original EVPFFT formulation for polycrystals by Lebensohn *et al.* [22], to be able to consider residual thermal strains present in the material, e.g., those measured by ff-HEDM.

In this work, the local CRSS of each slip system was incremented every strain step at each point $\{\mathbf{x}\}$ as follows:

$$\Delta \bar{\tau}^\alpha(\mathbf{x}) = \frac{d\bar{\tau}^\alpha(\mathbf{x})}{d\Gamma(\mathbf{x})} \sum_{\beta} h^{\alpha\beta} \dot{\gamma}^\beta(\mathbf{x}), \tag{5}$$

where $\Delta \bar{\tau}^\alpha(\mathbf{x})$ is the CRSS increment of slip system α , $h^{\alpha\beta}$ is the latent hardening of slip system α due to hardening of slip system β , $\dot{\gamma}^\beta(\mathbf{x})$ is the shear strain rate of slip system β , and $\Gamma(\mathbf{x})$ is the accumulated slip of all slip systems. The CRSS was scaled using a Voce hardening law given by:

$$\bar{\tau}^\alpha(\mathbf{x}) = \tau_0 + (\tau_1 + \theta_1 \Gamma(\mathbf{x})) \left[1 - \exp\left(-\frac{\theta_0}{\tau_1} \Gamma(\mathbf{x})\right) \right], \tag{6}$$

where τ_0 , τ_1 , θ_0 , and θ_1 are empirically determined Voce hardening law parameters. The latent and self-hardening coefficients $h^{\alpha\beta}$ for all slip system interactions were, by default, set to unity (i.e., no latent or self-hardening was considered).

The determination of equilibrated stress and compatible strain fields that locally fulfill the local constitutive relation in Eq. (3) is based on an *augmented Lagrangian* (AL) scheme, which is a numerically advantageous version of Moulinec-Suquet’s original basic scheme for composites [23] (subsequently extended to viscoplastic (VP) polycrystals [24]). This AL scheme was originally proposed for composites [25], then further broadened to (rigid) VP [26] and elasto-viscoplastic (EVP) polycrystals [22] to solve the above problem using Green’s functions and Fourier transforms.

As for every numerical scheme based on the Moulinec-Suquet formulation, C^0 is adopted as the stiffness of a linear reference medium and used to define a *polarization field* φ_{ij} at iteration (n) in the grid points $\{\mathbf{x}\}$ as follows:

$$\varphi_{ij}^{(n)}(\mathbf{x}) = \lambda_{ij}^{(n)}(\mathbf{x}) - C_{ijkl}^0 \varepsilon_{ij}^{(n)}(\mathbf{x}), \tag{7}$$

where—in the context of the AL method— $\lambda_{ij}^{(n)}(\mathbf{x})$ is a non-equilibrated stress/Lagrange multiplier field. With $\varphi_{ij}^{(n)}(\mathbf{x})$ known, the fluctuation field of the compatible strain field at iteration $n + 1$ is calculated in Fourier space as:

$$\begin{aligned} \hat{\varepsilon}_{ij}^{(n+1)}(\xi) &= \frac{1}{2} \left[\hat{\Gamma}_{ijkl}(\xi) \right. \\ &\quad \left. + \hat{\Gamma}_{jikl}(\xi) \right] \hat{\varphi}_{kl}^{(n)}(\xi), \\ \forall \xi \neq \mathbf{0} \text{ and } \hat{\varepsilon}_{ij}^{(n+1)}(\mathbf{0}) &= 0, \end{aligned} \tag{8}$$

where the Fourier transform (indicated by “^”) of the Green operator, $\hat{\Gamma}_{ijkl}(\xi)$, is given by:

$$\hat{\Gamma}_{ijkl}(\xi) = -\xi_j \xi_l \hat{G}_{ik}(\xi) \text{ with } \hat{G}_{ik} = \left[\xi_j \xi_l C_{ijkl}^0 \right]^{-1}. \tag{9}$$

With $\lambda_{ij}^{(n)}$ known, and $\varepsilon_{ij}^{(n+1)}$ obtained through Eq. (2) and anti-transforming Eq. (8), the residual R_k is defined as the difference between the two pairs of stress fields (the

equilibrated σ_{ij} and non-equilibrated λ_{ij}) and strain fields (the compatible ε_{ij} , and the incompatible e_{ij} , which is constitutively related to λ_{ij}) and nullified:

$$\begin{aligned} R_k(\sigma^{(n+1)}) &= \sigma_k^{(n+1)} + C_{kl}^0 e_l^{(n+1)}(\sigma^{(n+1)}) - \lambda_k^{(n)} \\ &\quad - C_{kl}^0 \varepsilon_l^{(n+1)} = 0, \end{aligned} \tag{10}$$

where contracted (Voigt) notation is used for symmetric tensors. This nonlinear system is solved using a Newton-Raphson (N-R) scheme:

$$\sigma_k^{(n+1,j+1)} = \sigma_k^{(n+1,j)} - \left(\frac{\partial R_k}{\partial \sigma_l} \Big|_{\sigma^{(n+1,j)}} \right)^{-1} R_l(\sigma^{(n+1,j)}), \tag{11}$$

which gives the ($j + 1$)-guess for the stress field $\sigma_k^{(n+1)}$. Using the constitutive relations in Eqns. (3) and (4), the Jacobian in the above expression can be approximated by:

$$\begin{aligned} \frac{\partial R_k}{\partial \sigma_l} \Big|_{\sigma^{(n+1,j)}} &\simeq \delta_{kl} + C_{kq}^0 C_{ql}^{-1} \\ &\quad + (\Delta m \dot{\gamma}_0) C_{kq}^0 \sum_{s=1}^{N_s} \frac{m_q^s m_l^s}{\tau^s(\sigma^{(n+1,j)})} \\ &\quad \left(\frac{\mathbf{m}^s : \boldsymbol{\sigma}}{\tau^s(\sigma^{(n+1,j)})} \right)^{n-1}, \end{aligned} \tag{12}$$

where the term $\partial \tau^s / \partial \sigma_j$, which depends on the specific functional form of the adopted hardening law, is neglected. Once convergence is achieved on $\sigma^{(n+1)}$, the new auxiliary stress field $\lambda_{ij}^{(n)}(\mathbf{x})$ is given by:

$$\lambda_{ij}^{(n+1)}(\mathbf{x}) = \lambda_{ij}^{(n)}(\mathbf{x}) + C_{ijkl}^0 \left(\varepsilon_{kl}^{(n+1)}(\mathbf{x}) - e_{kl}^{(n+1)}(\mathbf{x}) \right). \tag{13}$$

The iterative procedure ends when the relative error between the two pairs of stress and strain fields is below a specified tolerance.

While this algorithm solves constitutive equations for an applied macroscopic strain E_{ij} , the Challenge loading scenario has mixed boundary conditions, i.e., some components of strain and complementary components of the macroscopic stress Σ_{ij} are imposed. In these cases, the algorithm includes the following extra step after solving Eq. (10) for $\sigma_{ij}^{(n+1)}(\mathbf{x})$. If component Σ_{pq} is imposed, the corresponding ($n + 1$)-guess for component $E_{pq}^{(n+1)}$ is obtained as:

$$\begin{aligned} E_{pq}^{(n+1)} &= E_{pq}^{(n)} \\ &\quad + \alpha^{[kl]} \left(C_{pqkl}^0 \right)^{-1} \left(\Sigma_{kl} \right. \\ &\quad \left. - \langle \sigma_{ij}^{(n+1)}(\mathbf{x}) \rangle \right), \end{aligned} \tag{14}$$

where $\alpha^{[kl]} = 1$ if component Σ_{kl} is imposed and $\alpha^{[kl]} = 0$ otherwise, and $\langle \cdot \rangle$ indicates an average over the grid. Because

spectral methods solve constitutive equations within a periodic unit cell, the EVPFFT model inherently has periodic boundary conditions imposed on all surfaces. However, a secondary buffer zone (a material with infinite compliance, i.e., air) can be added to surfaces to “disconnect” the periodic boundary conditions of that surface. Only a few layers of buffer zone are required to remove periodic effects [26] and effectively model free surface boundary conditions.

In this work, the ability to simulate concatenated loading and unloading processes (e.g., see Fig. 2) was incorporated into the original EVPFFT code [22]. For each individual process, the history of local deformation is contained in the term $\varepsilon_{ij}^{p,r}(\mathbf{x})$. Therefore, the EVPFFT algorithm was extended by adding an external loop over processes (indicated in what follows by $[p,r]$), such that for every process, a combination of $E_{ij}^{[p,r]}$ and/or $\Sigma_{ij}^{[p,r]}$ components could be imposed. This extension was implemented in a serial code with an FFT algorithm that enforced the number of points along each dimension (i.e., 3D microstructure image dimensions) to be a power of two (2^n). This modified code was *required* to simulate the multiple loading processes to generate model predictions for the Challenge. Aside from this serial code, a parallelized implementation of the EVPFFT formulation, Micromechanical Analysis of Stress–Strain Inhomogeneities with Fourier transforms (MASSIF), was used for a post-Challenge material parameter optimization scheme described later on. MASSIF is simply a parallelized version of the base EVPFFT formulation that leverages the parallel Fastest Fourier Transform in the West (FFTW) [27] and Hierarchical Data Format version 5 (HDF5) [28] libraries. The FFTW library additionally handles arbitrarily sized grids, which removes the 2^n 3D microstructure image requirement imposed in the serial code.

Challenge-Submission Model (Blind Predictions)

To utilize the serial EVPFFT code, it was necessary to modify the dimensions of the microstructural volume provided by AFRL to conform to the 2^n image dimensions imposed by the FFT algorithm. To meet this dimensional requirement while retaining the majority of the microstructural volume, the original image dimensions of $305 \times 351 \times 312$ voxels were ultimately reduced to $256 \times 256 \times 256$ voxels by applying the following sequence of operations. First, the “Minimum Size” filter in DREAM.3D was applied to remove grains comprising fewer than 25 total voxels, which was well below the size of the smallest Challenge grain. This was (unnecessarily) done to remove very small grains that would be either removed or enlarged during subsequent downsampling. Next, the microstructure was cropped to 248 voxels on both the x and z -axes and subsequently downsampled by

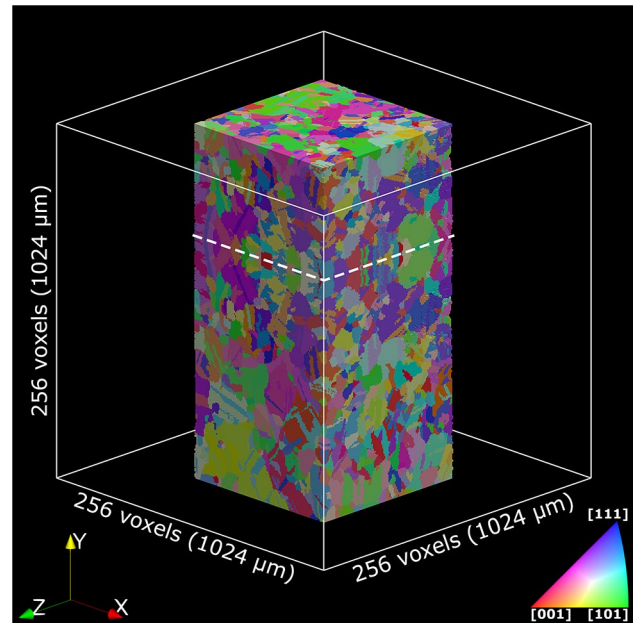


Fig. 3 Inverse pole figure (IPF) map of the mirrored microstructure geometry used in the Challenge-submission model. The mirroring plane is shown by the dashed white line. The gap between the microstructure and the extents of the simulation volume (outlined in white) comprises a buffer zone that serves to disconnect the periodic boundary conditions in the EVPFFT model to represent unconstrained surfaces

50% to reach image dimensions of $124 \times 175 \times 124$ voxels ($496 \times 700 \times 496 \mu\text{m}^3$). The cropping procedure primarily removed the secondary phase buffer zone; however, small surface portions of the primary phase were removed, including two surface Challenge grains where 10% and 4% of the voxels were removed. Next, a 66-voxel-thick border of buffer zone was added around the edges of the x - z plane to extend the x - and z -axes to 256 voxels. Finally, the top 81 voxels of the microstructure were mirrored across the top x - z plane to extend the y -axis to 256 voxels. Several Challenge grains were included as part of this mirrored region, but only the original portion of the microstructural volume was considered in the submission. In essence, the mirroring and extension of the buffer zone were completed solely to satisfy the 2^n dimension requirement, although the buffer zone is required to model free surface boundary conditions. Figure 3 shows the final mirrored $256 \times 256 \times 256$ voxel ($1024 \times 1024 \times 1024 \mu\text{m}^3$) microstructure.

The constitutive parameters were determined by fitting the simulated stress–strain curve to the experimental stress–strain curve provided for the Challenge specimen (including unloading). The stiffness tensor C_{ijkl} was populated with the three unique single-crystal elastic constants for IN625 (a face-centered cubic material) published by Wang *et al.* [29] (see Table 1).

Table 1 Single-crystal elastic constants for IN625 published by Wang et al. [29]

c_{11} [GPa]	c_{12} [GPa]	c_{44} [GPa]
243.3	156.7	117.8

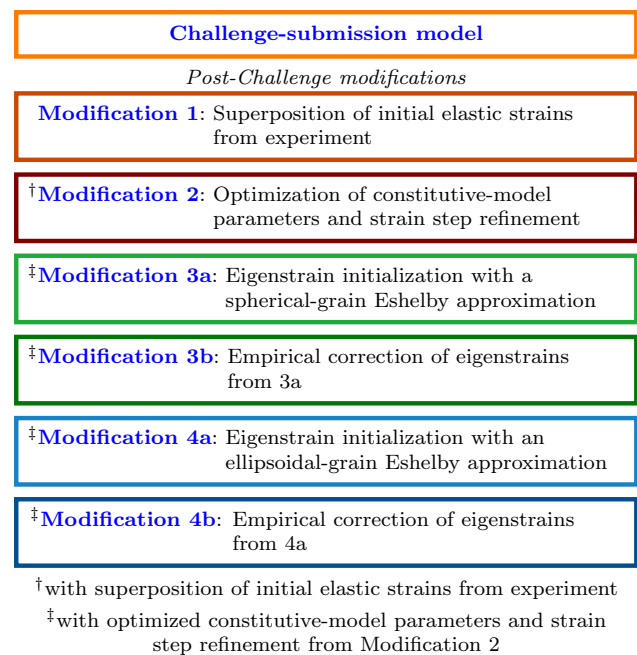
Table 2 Voce hardening model parameters used in the AFRL Challenge-submission model

τ_0 [MPa]	τ_1 [MPa]	θ_0 [MPa]	θ_1 [MPa]
143.0	50.0	1450.0	95.0

These elastic constants were found to provide a good macroscopic fit to the elastic portion of the curve and therefore required no modification. The Voce hardening law parameters in Eq. (6) were manually fit by iteratively adjusting parameters until the correspondence with the experimental data was deemed reasonable. Fitting was performed using a 50% resolution image of the microstructure to speed up computation time. This brute force technique led to a slight overprediction of the EVPFFT macroscopic response in the plastic region. The final Voce hardening law parameters used for the Challenge-submission model are given in Table 2.

Boundary conditions were defined in the EVPFFT model to emulate the displacement-controlled loading conditions in the tensile test (see Fig. 1). For all loading processes, uniform axial strain E_{yy} steps of 0.00025 mm/mm were imposed on the loading axis (y -axis). With these strain steps, the model reached stress states that were within 3% of the first three target stress states. The shear components of E_{ij} were set to zero, i.e., the volume average shear strain was nullified. The transverse components (xx and zz) of $\Sigma_{ij}^{[pr]}$ were prescribed to zero macroscopic stress for all processes. At axial strains of 0.0035 and 0.0050 mm/mm, the model was unloaded by -0.00022 mm/mm (in a single strain step) and subsequently reloaded; the model was unloaded a final time upon reaching 0.0100 mm/mm axial strain. These three unloading steps unloaded the volume by an average of 54.1 MPa (as opposed to the 50 MPa unloading performed during the experiment to avoid creep during each HEDM measurement in the plastic regime).

The final simulation was solved using the serial version of the EVPFFT code described in Sect. 3.1. An error tolerance of 10^{-5} was used as the convergence criteria for each strain step, which additionally satisfied compatibility and static equilibrium to the same tolerance [30]. The initial elastic strain field at S0 provided by AFRL was neglected, and no eigenstrain field was initialized (i.e., $\epsilon_{ij}^*(\mathbf{x}) = 0$ in Eq. (3)). The precipitate phase was also not considered in the model. The final Challenge-submission model required approximately 72 wall-clock hours to run on a 2018

**Fig. 4** Key of modifications made during post-challenge investigation. Color coding corresponds to Fig. 8

MacBook Pro. The final results for the blind predictions based on the Challenge-submission model are presented in Sect. 4.

Post-Challenge Modifications

Following the release of the experimental results, several modifications were explored to try and improve model performance. Although these modifications were performed with the knowledge of the experimentally measured strains, no modifications were made that required any information beyond what was initially provided for the AFRL Challenge. For an overview legend to the following modifications, see Fig. 4. Unless otherwise noted, the modifications carry forward to all subsequent model iterations. For example, when the microstructure geometry was changed, that change was reflected in all subsequent models. Additionally, if model parameters are not mentioned in subsequent sections, those respective parameters can be assumed to be the same as those given in Sect. 3.2.

Modification 1: Superposition of Initial Elastic Strains from Experiment

For the first modification, the initial strain field was included by simply adding it to the model predictions. As such, there were no changes to any model inputs relative to the Challenge-submission model. Mathematically, the superposition of the initial strain field is expressed as:

$$\varepsilon_{ij}^{e,\text{mod}}(g, S) = \varepsilon_{ij}^{e,\text{fit}}(g, S) + \varepsilon_{ij}^{e,0}(g), \quad (15)$$

where $\varepsilon_{ij}^{e,\text{mod}}$ is the predicted (modified) elastic strain tensor, $\varepsilon_{ij}^{e,0}$ is the initial elastic strain tensor provided by AFRL for a given Challenge grain, $\varepsilon_{ij}^{e,\text{fit}}$ is the predicted elastic strain tensor from the Challenge-submission model, and g and S represent the Challenge grain and target stress state, respectively. This constituted a naïve approach to incorporating the initial elastic strain field because compatibility was no longer achieved, but it was a simple first step in utilizing the initial strain state.

Modification 2: Optimization of Constitutive-Model Parameters and Refinement of Strain Steps

The intent of Modification 2 was to more accurately represent the macroscopic stress–strain response from the experiment (without adding model complexity relative to the Challenge-submission model) by optimizing the constitutive model parameters and refining the applied strain steps. Prior to optimizing the material parameters and refining the strain steps, the microstructure geometry was modified to make more efficient use of the 2^n volume dimension requirement discussed earlier. The original microstructural image was downsampled non-uniformly, resulting in *cuboidal* voxels with physical dimensions of $2.10 \times 2.74 \times 2.10 \mu\text{m}^3$. These voxel dimensions were chosen to reduce the y -axis image dimension from 312 to 256 voxels and slightly reduce the z - and x -axis image dimensions from the original image dimensions. Finally, several layers of buffer zone contained in the original dataset provided by AFRL were cropped around the microstructure to obtain a final 3D microstructure image with dimensions of $256 \times 256 \times 256$ voxels ($538 \times 702 \times 538 \mu\text{m}^3$). A minimum of eight voxels of buffer zone was left on the x - y and y - z surfaces to model the unconstrained boundary conditions. This image modification allowed for much more of the simulated volume to comprise voxels of interest (primary phase, non-mirrored voxels) rather than extraneous data (see Fig. 3). Using the same $256 \times 256 \times 256$ voxel volume dimensions, there were 4.36 times as many voxels of interest in the microstructure image of Modification 2 compared to the simulation volume used in the Challenge-submission model. Thus, the problem size (i.e., runtime) was the same in both cases, but the cuboidal-voxel microstructure had a higher effective resolution, as depicted in Fig. 5. It is noted that a convergence study was later carried out to assess the impact of 3D image resolution on both global and local response metrics, and it was found that, while the image modification here makes better use of the $256 \times 256 \times 256$ voxel image dimensions compared to the Challenge-submission model, the modification does not, on its own, impact the predictions. In other words, all models

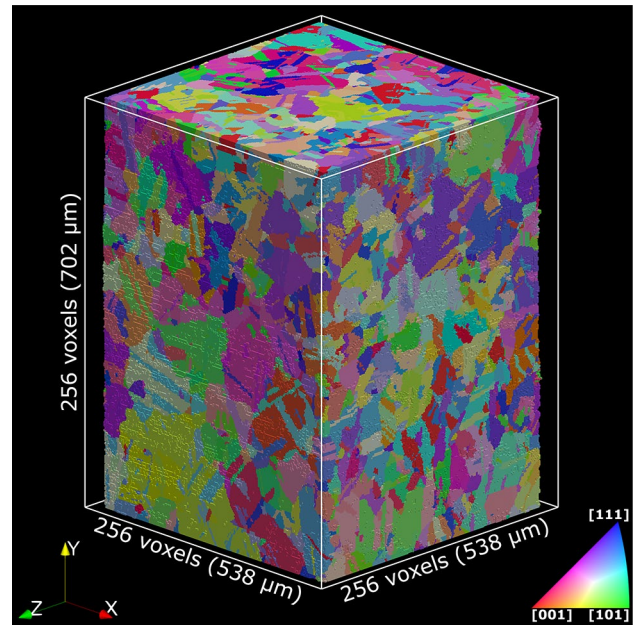


Fig. 5 Inverse pole figure (IPF) map of the microstructure geometry used in models corresponding to Modifications 2 through 4b. The slight gap between the microstructure and the extents of the simulation volume (outlined in white) comprises a buffer zone that serves to disconnect the periodic boundary conditions in the EVPFFT model to represent unconstrained surfaces

described in this manuscript (including the Challenge-submission model) were found to have adequate resolution to achieve convergence with respect to voxel size. Details of the convergence study are provided in Appendix A.

Next, a material parameter optimization scheme was implemented to improve the fit of the macroscopic response of the EVPFFT model through a method of least squares. The four Voce hardening law parameters in Eq. (6) were optimized by minimizing the mean squared error (MSE) between the model and experimental stress–strain curves calculated by:

$$\text{MSE} = \frac{1}{N} \sum_{n=1}^N \sqrt{(\sigma_n^{\text{fit}} - \sigma_n^{\text{exp}})^2}, \quad (16)$$

where N is the total number of experimental data points, σ_n^{fit} is the predicted macroscopic axial stress of the EVPFFT model at the experimentally applied strain of point n calculated with cubic interpolation, and σ_n^{exp} is the macroscopic axial stress of the experimental data at the applied strain of point n . Powell's method [31] implemented in SciPy [32] was used to minimize the MSE and performed a full EVPFFT simulation for each optimization iteration. Several different optimization strategies with and without numerical differentiation were tested, and although Powell's method only converges to local minima, it performed the best of

Table 3 Voce hardening law parameters determined by minimizing the mean squared error between the experimental and simulated macroscopic stress–strain response

τ_0 [MPa]	τ_1 [MPa]	θ_0 [MPa]	θ_1 [MPa]
138.95	39.44	1579.89	14.24

all optimization strategies, provided a good initial guess for the parameters was supplied. Additionally, a hierarchical optimization scheme was used (e.g., see Ref. [33]) in which the parameters were optimized for a series of microstructure resolutions. In this case, the parameters were first optimized using a 25% resolution microstructure image to get a “rough” estimate of the parameters. The parameters were then reoptimized on a 50% resolution microstructure image using the previously optimized parameters as an initial guess. For runtime reasons, MASSIF (the parallelized implementation of the EVPFFT model) was used for the optimization procedure. Due to current limitations in MASSIF, the monotonic stress–strain response (i.e., without unloading/reloading) was used to fit the parameters. The total optimization process took less than 24 wall-clock hours (roughly 250 iterations of 1.5 wall-clock minutes and 100 iterations of 10 wall-clock minutes for the 25% and 50% resolution microstructures, respectively) with an AMD 7702P 64-core processor with 256 gigabytes of memory from the Center for High Performance Computing at the University of Utah. The optimized Voce hardening law parameters determined from this optimization scheme are given in Table 3.

After the Voce hardening law parameters were fit, the applied boundary conditions were refined to more closely achieve the target stress states at which ff-HEDM data were collected. Axial strain E_{yy} step values were iteratively adjusted to reach model states that were very similar to the target stress states. For the first three target stress states (S1–S3), the EVPFFT volume-averaged axial stress values were all within 0.2% of the target stress states compared to the 3% error in the Challenge-submission model. For the final three target stress states (S4–S6), instead of unloading by a constant strain step, the volume was unloaded by specific strain steps to reach volume-averaged stress values of approximately 309, 323, and 353 MPa, corresponding to the mean sample stress during the hold period of the ff-HEDM measurement. This was deemed necessary, as the experimentally collected stress–strain data was relatively noisy, and unloading by 0.00022 mm/mm in the model did not achieve the target stress states as well as unloading to specific macroscopic stress values. As with the previous modification, the initial elastic strains provided by AFRL were accounted for using a simple superposition. Figure 6 provides a visual comparison between the experimental

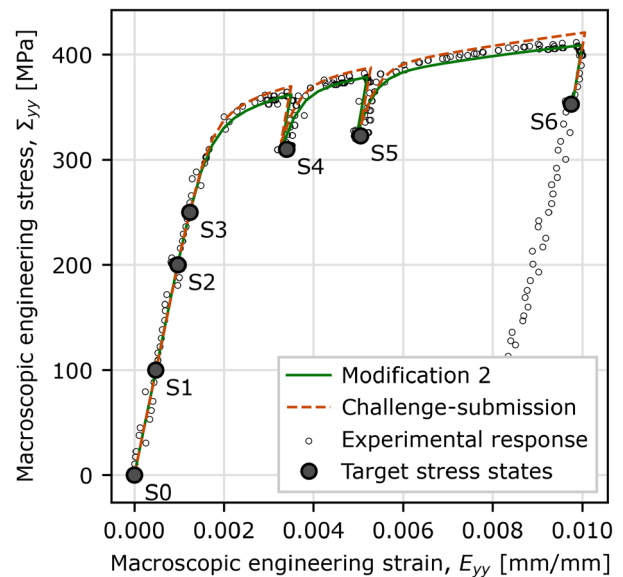


Fig. 6 Macroscopic engineering stress–strain response of the tensile specimen compared to the predicted responses of the Challenge-submission and Modification 2 models. The initial state (S0) and six target stress states (S1–S6) at which the sample was held for ff-HEDM data collection are indicated

data and the macroscopic fit of the model before and after implementing the changes described in this section.

Modification 3a: Eigenstrain Initialization with a Spherical-Grain Eshelby Approximation

The intent of Modification 3 is to account for initial elastic strains by assigning a nonzero eigenstrain field. The microstructural image, constitutive parameters, and EVPFFT boundary and solver conditions remain unchanged from the conditions described in Sect. 3.3.2. In this modification, instead of simply adding the initial elastic strain tensors of each grain to the model predictions, a nonzero eigenstrain field ($\epsilon_{ij}^*(\mathbf{x}) \neq 0$ in Eq. (3)) was initialized. To calculate the eigenstrain field, an Eshelby approximation was used to convert the elastic strain field on a grain-by-grain basis. The Eshelby approximation is based on the known tensorial relationship between a uniform elastic strain tensor ϵ_{ij}^e and uniform eigenstrain tensor ϵ_{ij}^* of an inclusion (i.e., grain) embedded within an isotropic, infinite, homogeneous matrix, defined by:

$$\epsilon_{ij}^* = (S_{ijkl} - I_{ijkl})^{-1} \epsilon_{kl}^e, \quad (17)$$

where S_{ijkl} is the uniform fourth-rank Eshelby tensor calculated from a known analytical solution for a given inclusion shape and elastic stiffness [34] and I_{ijkl} is the fourth-rank identity matrix. An elastic self-consistent approximation [35] of a cubic polycrystal with random texture and the

single-crystal elastic constants given in Table 1 was used to calculate Poisson's ratio, $\nu = 0.312$. In the eigenstrain calculation for Modification 3, all grains were assumed to be spherical, which greatly simplifies the calculations of the values within the Eshelby tensor to a single equation (Eq. 11.21 in Ref. [34]) and requires no parameterization of complex grain shapes. Nonzero eigenstrains were defined only for the 28 Challenge grains as the initial elastic strains from the experiment were provided for only those grains. There is only a small macroscopic effect of initializing an eigenstrain field [21], and a negligible effect in this case, given that only the eigenstrains in the 28 Challenge grains are nonzero.

Interestingly, the majority of the Challenge grains had an initial negative hydrostatic elastic strain according to the ff-HEDM measurements. When the modeled grains are initialized with this net negative strain, the grains require more applied elastic strain to yield than if there was no net initial strain. This results in general overpredictions of the elastic strains in these grains. In order to deal with this, the mean initial elastic strain tensor was subtracted from the total initial elastic strain tensor for each grain prior to calculating the eigenstrain tensor, as follows:

$$\varepsilon_{ij}^* = (S_{ijkl} - I_{ijkl})^{-1} (\varepsilon_{kl}^e - \bar{\varepsilon}_{kl}^e), \quad (18)$$

where $\bar{\varepsilon}_{kl}^e$ is the mean initial elastic strain tensor, i.e., the component-wise average of all the initial elastic strain tensors given for the Challenge grains. This step was performed in order to shift the components of the mean initial elastic strain tensor to be zero and is very similar to what Tari *et al.* [36] did to negate the effect of an initial tensile load. The mean initial elastic strain tensor was then reintroduced into the predictions by adding it to the model output at all states via:

$$\varepsilon_{ij}^{e,\text{mod}}(g, S) = \bar{\varepsilon}_{ij}^e + \varepsilon_{ij}^{e,\text{fft}}(g, S), \quad (19)$$

where $\varepsilon_{ij}^{e,\text{mod}}$ is the final predicted (modified) elastic strain tensor and $\varepsilon_{ij}^{e,\text{fft}}$ is the elastic strain tensor calculated from the EVPFFT model for each grain, g , and stress state, S . A follow-on modification, referred to as Modification 3b, is described in Sect. 3.3.5.

Modification 4a: Eigenstrain Initialization with an Ellipsoidal-Grain Eshelby Approximation

Modification 4 improves upon the aforementioned eigenstrain estimation by treating the Challenge grains as ellipsoidal, rather than spherical, in the Eshelby approximation. The ellipsoidal-grain assumption is novel in terms of initializing elastic strain fields in the EVPFFT modeling method and is reported for the first time here. This modification used

the same equations, process, and input parameters as in Sect. 3.3.3, except that Eshelby's tensor was calculated using the solution for an ellipsoidal inclusion [37] rather than the simplified case of a spherical inclusion. The ellipsoidal parameters of each grain were calculated using the "Find Feature Shapes" filter in DREAM.3D [19], which calculates the principal semi-axis lengths of the best-fit ellipsoid for an individual grain using a moment of inertia method described by Groeber *et al.* [38]. The semi-axis lengths and orientation of the best-fit ellipsoid are then used to calculate Eshelby's tensor in the ellipsoid reference frame. These calculations are described in more detail in Appendix B. The same subtraction and reintroduction of the mean initial elastic strain tensor described by Eqns. (18) and (19) was employed as before. A follow-on modification, referred to as Modification 4b, is described next.

Modifications 3b and 4b: Empirically Corrected Eigenstrains

Due to the assumptions associated with isotropy, grain shape, and homogeneity in the Eshelby approximation, there are inherent errors in the calculated eigenstrains that can be empirically corrected. Pokharel and Lebensohn [21] proposed adding a scalar correctional matrix, β_{ij} , to the eigenstrains calculated by Eq. (17) to alleviate disparities caused by these assumptions. Due to the change of basis incorporated in the ellipsoidal Eshelby approximation, the correctional matrix *must* be applied after the eigenstrains are calculated in the global reference frame, i.e.,

$$\varepsilon_{ij}^{*,c} = \beta_{ij} \varepsilon_{ij}^* \quad \text{no sum over } ij, \quad (20)$$

where $\varepsilon_{ij}^{*,c}$ is the corrected eigenstrain tensor calculated by the Hadamard (element-wise) product between the correctional matrix β_{ij} and the uncorrected eigenstrain tensor ε_{ij}^* in the global reference frame. This implementation has the same effect as in Ref. [21], but the correctional matrix is simply applied further along in the calculations. The correctional matrix is symmetric due to the symmetry of the strain tensor and thus contains six unique scalar constants. For an in-depth process of calculating the constants in the correctional matrix, see Appendix A in Ref. [36]. Succinctly, this process involves (1) initializing the EVPFFT model with the calculated eigenstrain field, (2) applying a negligible strain step (10^{-6} mm/mm) and equilibrating the stress and strain fields, (3) performing simple linear regressions between the six unique components of the initial elastic strain tensors and the corresponding components of the equilibrated elastic strain tensors for all grains, and (4) calculating the six correctional values in β_{ij} required to change the slopes of the best-fit linear-regression curves to unity (i.e., to achieve a perfect fit). Correctional matrix values were calculated and applied to the eigenstrain fields from

Table 4 Calculated correctional matrix (β_{ij}) values for both spherical and ellipsoidal eigenstrain grain-shape assumptions. Correctional values closer to unity indicate that less empirical correction is required.

Shape assumption	β_{11}	β_{22}	β_{33}	β_{23}	β_{13}	β_{12}	β_{avg} (%)	R^2_{avg}
Spherical	1.07	0.78	1.51	0.86	1.23	1.06	20.5	0.873
Ellipsoidal	1.03	1.02	1.09	0.93	1.10	1.03	5.7	0.925

The β_{avg} column calculates the average percent correction (with respect to 1) of each row. The average coefficient of determination (R^2_{avg}) from the six linear regressions is also given

both the spherical (Modification 3a) and ellipsoidal (Modification 4a) Eshelby approximations. Supplementary Figs. S-1 and S-2 (refer to Electronic Supplementary Material) visually show this calculation process for the Modification 3a and 4a models. Subsequently, *two* EVPFFT models (named Modification 3b and 4b) were initialized with these corrected eigenstrain fields and analyzed. The six correctional matrix values from this linear regression process are given in Table 4, along with the average R^2 value (i.e., the average correlation between the initial and equilibrated elastic field).

We have recently implemented the previously presented methods for calculating the eigenstrain field from the initial elastic strain field into DREAM.3D as the “Compute Eigenstrains by Feature (Grain/Inclusion)” filter. For each grain, the filter computes the uniform eigenstrain tensor using the elastic strain tensor, Poisson’s ratio, the best-fit ellipsoid grain shape, and optionally, the correctional matrix. This filter is included in the main DREAM.3D distribution on all platforms as of version 6.5.151 which can be downloaded from <http://dream3d.bluequartz.net/>.

Results

To analyze the performance of each model, three types of analyses are performed. The first is to simply use the Challenge grading metric (described in Sect. 2.3) to provide an overall comparison among models. The second is a simple linear regression between the predicted and experimental elastic strain tensor components at the six target stress states for the 28 Challenge grains to provide a more refined comparison among models. The final analysis is a mean error method that gives insight into trends of over- and underprediction of specific strain components, i.e., model bias. These three methods combine to give valuable insight into model trends and performance. Figure 7 provides an example of the micromechanical anisotropy and heterogeneity observed in the simulations. A short animation showing the evolution of the axial elastic strain field with applied macroscopic load for the Modification 4a model is given in the Electronic Supplementary Material.

Overall Model Performance

To compare model predictions, the Challenge L2-norm error grading metric given in Eq. (1) is used. Since this metric uses an L2 norm, strain components with larger errors dominate the L2-norm error of each grain. Generally, this implies that normal strain components have a larger effect on the total L2-norm error than shear strain components. This is because the normal strains are generally larger in magnitude and thus larger in absolute error than the shear components. For all models, Fig. 8 gives the L2-norm error for each target stress state along with the sum of the errors from each state, or the total L2-norm error.

To statistically compare model predictions to *each other*, an adjusted total L2-norm error of each model was calculated using the Modification 4a model instead of the experimentally collected data as a reference (i.e., $\epsilon_k^{\text{e,exp}}$ in Eq. (1) was taken from the Modification 4a predictions). A one-way

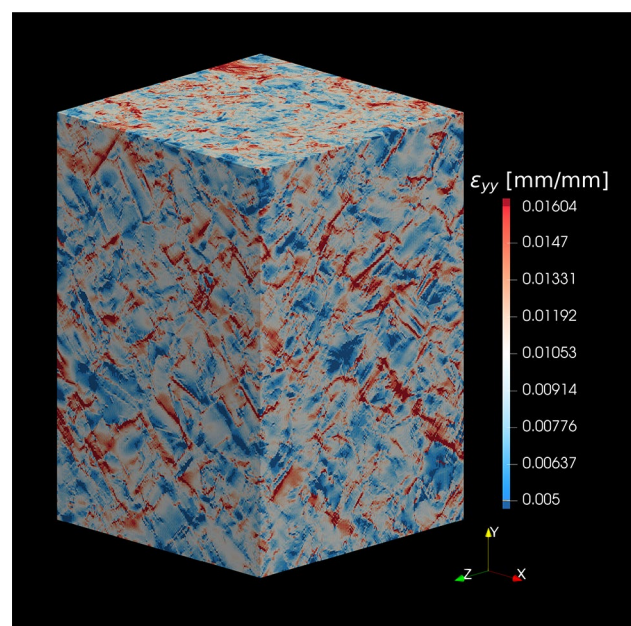


Fig. 7 Total axial strain field ($\epsilon_{yy}(\mathbf{x})$) of the Modification 4a model at target stress state S6. For visual clarity, the x - y and y - z surfaces have been cropped slightly to remove surface artifacts. The color scale bounds are between the 2nd and 98th percentiles of the axial strain field

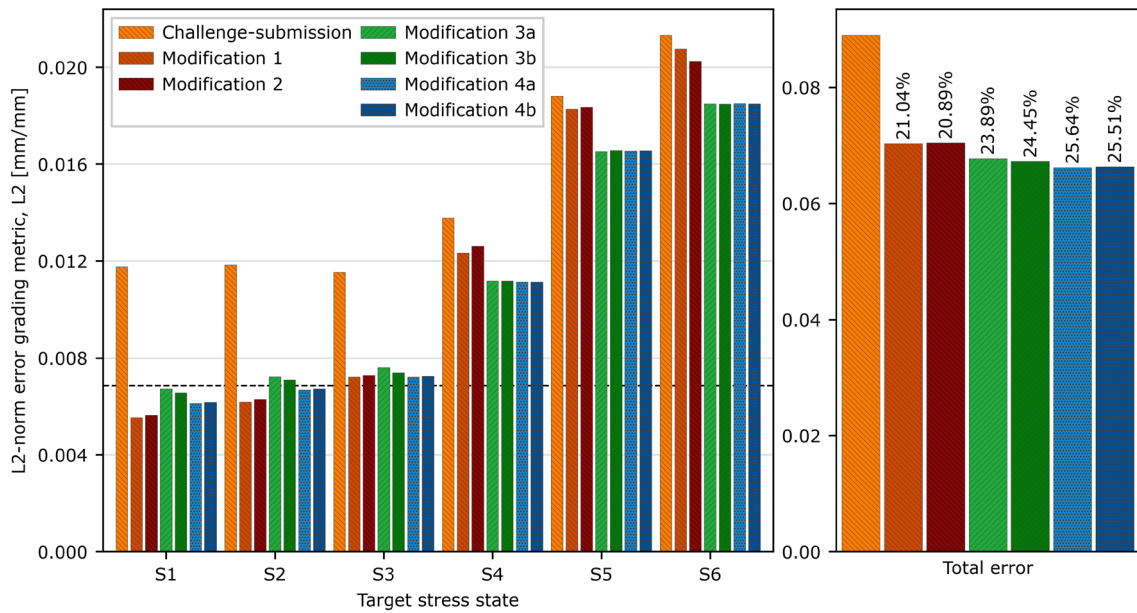


Fig. 8 L2-norm error at the six target stress states calculated using only the inner summation in Eq. (1) (left) and total L2-norm error (right) for the different models. For all post-submission models, the percent decrease in total error relative to the Challenge-submission

model is labeled above each bar. The black horizontal line indicates the L2-norm error for a constant 100 μe offset corresponding to the standard resolution of ff-HEDM [39]

analysis of variance (ANOVA) test was performed, which showed a significant difference between the adjusted total L2-norm error of the models, $F(6, 1169) = 242.4, p < 0.001$. A post hoc Tukey test [40] revealed that 18 of 21 pairs of these adjusted total L2-norm errors were significantly different from one another at a significance level of $p_{\text{adj}} < 0.05$ ¹. The test was unable to find statistically significant differences between the L2-norm errors of only three model pairs: Modification 4a vs. Modification 4b, Modification 3a vs. Modification 3b, and Modification 1 vs. Modification 2.

Linear Regression

The second method for model comparison is to plot the predicted versus experimental values of each of the six elastic strain components at each of the six target stress states for the 28 Challenge grains. As an example, Fig. 9 shows the Challenge-submission versus experimental values of the axial elastic strain component (ϵ_{yy}^e) for the 28 Challenge grains at target stress state S4. Simple linear regression was performed, and the coefficient of determination (R^2) and slope (m) are given in the plot along with the mean error (ME), which is defined in Sec. 4.3.

The linear regression shown in Fig. 9 is then performed for all six strain components at all six target stress states

for a total of 36 different plots. For each of the seven models investigated, the 36 plots are given in supplementary Figs. S-3–S-9 (refer to Electronic Supplementary Material) as single-image plot matrices. To simplify the presentation

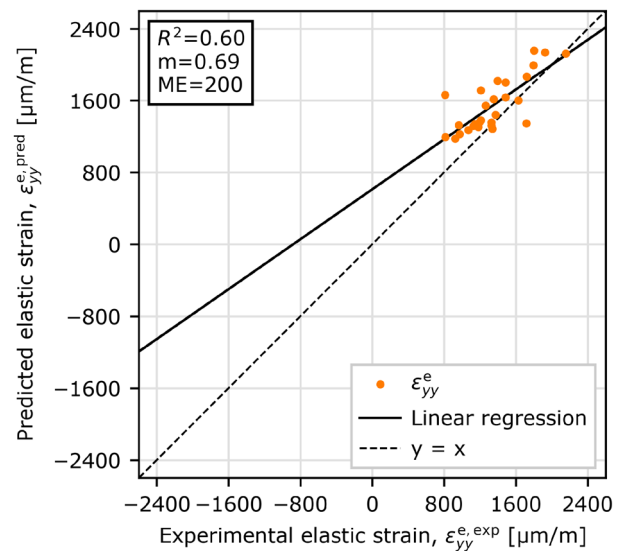


Fig. 9 Challenge-submission model predicted versus experimental axial elastic strain ϵ_{yy}^e at target stress state S4. The line $y = x$ indicates the ideal 1:1 fit. The legend gives the coefficient of determination (R^2) and slope (m) of the regression line as well as the mean error (ME)

¹ p_{adj} is the p -value adjusted for multiple comparisons.

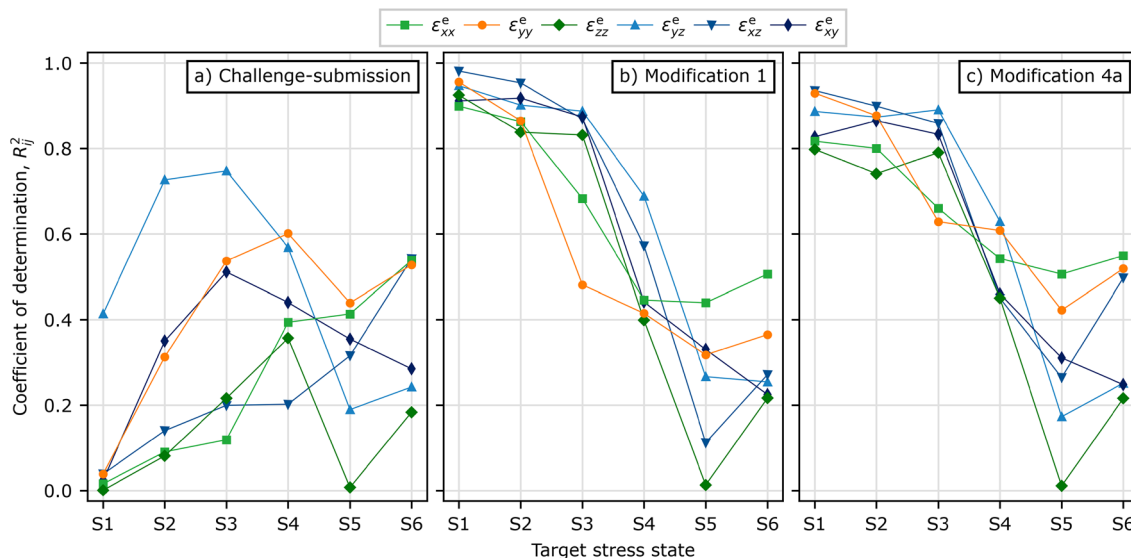


Fig. 10 Performance plots (relative to experiment) of the **a** Challenge-submission, **b** Modification 1, and **c** Modification 4a model predictions, where the 36 R^2 values in each plot are extracted from

the 6×6 plot matrices in supplementary Figs. S-3, S-4, and S-8, respectively (refer to Electronic Supplementary Material)

of the results presented herein, the 36 plots are compressed into 36 points on a single plot by extracting the R^2 values. Figure 10 shows the compressed R^2 plots for three of the models (Challenge-submission, Modification 1, and Modification 4a), which are representative of the range of L2-norm errors among the seven models investigated. Note that in these R^2 plots, Modification 1 (Fig. 10b) is representative of Modification 2, and Modification 4a (Fig. 10c) is representative of Modifications 3a, 3b, and 4b.

Mean Error and Model Bias

The final metric used to evaluate each model is the mean error (ME) between the predicted and experimental elastic strain tensor components at each of the six target stress states. The ME provides the average over- and underprediction, or *bias* of the model, and is calculated as follows:

$$ME_{ij} = \frac{1}{N} \sum_{g=1}^N (\epsilon_{ij}^{e,pred} - \epsilon_{ij}^{e,exp}), \tag{21}$$

where $\epsilon_{ij}^{e,pred}$ and $\epsilon_{ij}^{e,exp}$ are, respectively, the predicted and experimentally measured elastic strain tensor components for each of the $N = 28$ Challenge grains, g . From Eq. (21), a positive ME indicates an overprediction, and a negative ME indicates an underprediction. Note that the ME is not an absolute error metric; for example, if $\epsilon_{ij}^{e,exp}$ is negative, an overprediction of $\epsilon_{ij}^{e,pred}$ generally underpredicts the magnitude of the strain component. The ME is also the same as the average vertical difference between the data points and the

line $y = x$ in all regression plots and is equal to the intercept of the regression line when the slope is unity. Figure 11 shows the ME plotted for the Challenge-submission, Modification 1, Modification 2, and Modification 4a models, which represent the range of ME values observed among the seven models investigated.

An important note from these ME plots is the large underprediction seen in the yz -component of shear strain in the plastic regime. Singling out the Challenge-submission model, almost half of the ϵ_{yz}^e underprediction at S6 is attributed to a single outlier grain (grain ID 8445), for which the yz -component is underpredicted by 2098 $\mu\epsilon$, contributing to the large negative ME and confidence interval. It is emphasized that this grain is an outlier in the *measured* strains and has a magnitude 3.8 times higher than the next largest shear strain magnitude at S6 based on the ff-HEDM measurements. Therefore, this outlier grain causes a similar trend in all other models.

There are some numerical values worth extracting from Fig. 11 for future discussion. Looking specifically at the axial elastic strain component ϵ_{yy}^e at S6, the Challenge-submission model (Fig. 11a) ME is 369 $\mu\epsilon$ or a $(26.4 \pm 7.3)\%$ overprediction, the Modification 1 model (Fig. 11b) ME is 260 $\mu\epsilon$ or a $(18.6 \pm 9.2)\%$ overprediction, the Modification 2 model (Fig. 11c) ME is 185 $\mu\epsilon$ or a $(13.3 \pm 9.0)\%$ overprediction, and the Modification 4a model (Fig. 11d) ME is 184 $\mu\epsilon$ or a $(13.2 \pm 7.2)\%$ overprediction.

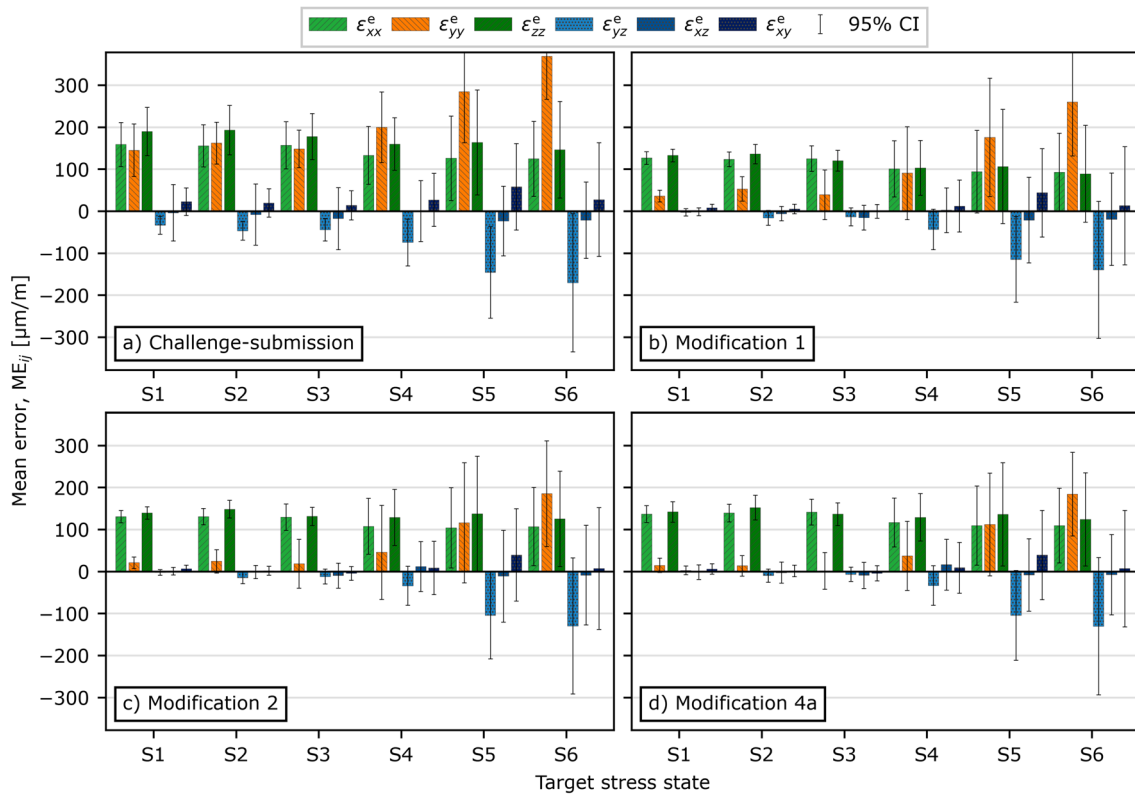


Fig. 11 Mean error plots (relative to experiment) for the **a** Challenge-submission, **b** Modification 1, **c** Modification 2, and **d** Modification 4a model predictions. The error bars indicate the 95% confidence interval (CI)

Discussion

From the results presented, there are several key trends, takeaways, and opportunities for future improvements that are identified for predicting micromechanical response using the EVPFFT modeling method. The reader is referred to Fig. 4 for a summary of the key changes incorporated in each post-Challenge modification model. It is again noted that the first three target stress states (S1–S3) represent macroscopic states in the elastic regime, and the final three target stress states (S4–S6) represent macroscopic states in the plastic regime (see Fig. 2).

Analysis of Model Trends

From the overall error comparisons among the seven models (Fig. 8), there are two interesting trends observed. First, all of the models exhibit a steady decrease in performance with accumulated plastic strain. This observation is similar to results reported by Tari *et al.* [36] for a validation of the EVPFFT method on a Ti-7Al polycrystal. This trend is expected given that plasticity is a much harder problem to model than elasticity, highlighting the need for continually improving plasticity modeling efforts. Second, the

post-Challenge model performance in the elastic regime (S1–S3) shows a very low L2-norm error for all models in comparison with both the Challenge-submission model and the experimental measurements. This error is below the typical strain resolution reported for ff-HEDM [39], thus demonstrating the accuracy of the EVPFFT model predictions in the elastic regime.

From the ME plots in Fig. 11, there are a number of noteworthy model-bias improvements made by post-Challenge modifications. First, the improvements made to axial (yy) strain bias are examined, specifically at target stress state S6. In comparison with the Challenge-submission model (Fig. 11a), the Modification 1 model (Fig. 11b) reduces the S6 axial-strain overprediction by 30% through the superposition of the initial elastic strain field. This superposition lowers the overprediction because the initial strain state in the majority of the Challenge grains is compressive (i.e., negative). The Modification 2 model (Fig. 11c) then further reduces the S6 axial overprediction—by 50% compared to the Challenge-submission model—due to the optimized macroscopic stress–strain response (Fig. 6). The ME plot of the Modification 4a model (Fig. 11d) is very similar to the Modification 2 model because the initialization of an eigenstrain field has only a minor effect on the macroscopic

stress–strain response [21], which in turn only slightly affects the ME. However, the removal of the average initial strain in the eigenstrain field calculations and subsequent re-addition (Eqns. (18) and (19)) is necessary for this to be true *if* there is a nonzero mean initial strain state in the target grains. Beyond the model-to-model differences in ME, there is one major trend observed in the axial-strain ME for *all* models in the plastic regime. Specifically, from Fig. 11, the axial elastic strains are increasingly overpredicted with accumulated plastic strain, regardless of the model. Given that this increase in model bias occurs in the plastic regime, the phenomenon that causes this is inherently plasticity-based. There are a multitude of physical, experimental, and modeling factors that could cause such a trend to occur, which remains the topic of ongoing investigation.

Continuing to examine the ME plots in Fig. 11, there is another important trend seen in the transverse (xx and zz) strain biases of all models. Looking specifically at the post-Challenge modification models in Fig. 11b–11d, there is a nearly constant overprediction, on average, of $130 \mu\epsilon$ in both transverse strain components for the first three target stress states (S1–S3) before slightly decreasing at each of the final three target stress states (S4–S6). The transverse strains are overpredicted slightly less (more apparent in the xx than the zz component) at the final three target stress states due to the axial-strain overprediction. The Poisson effect negatively correlates the axial and transverse components of strain to one another; thus, when the ME of the axial strains increases, the ME of the transverse strains must *decrease*. Because of this, if there were no overprediction of the axial yy strain, the transverse-strain overprediction of approximately $130 \mu\epsilon$ would remain constant at all six target stress states. Given that the transverse strains are negative due to the Poisson effect, an overprediction or positive ME in these components indicates an *underprediction* in strain magnitude. In other words, both transverse strain components are consistently about $130 \mu\epsilon$ more negative in the experimental data than all model predictions at all target stress states. If this bias were attributed to the single-crystal elastic constants, the bias would *not* be constant, and instead would vary with load. The cause of this constant transverse-strain bias is again a topic of ongoing investigation, but given that the bias is constant at all target stress states, the phenomenon that causes this most likely occurs before or during the first ff-HEDM measurement.

Focusing specifically on the L2-norm errors and R^2 values in Figs. 8 and 10, there are several trends and comparisons to be made between model performance. First, when the initial elastic strain field is superposed onto the Challenge-submission model predictions (Modification 1), the R^2 values in the elastic regime show that the predictions improve from almost no correlation to a very high correlation (Fig. 10a versus Fig. 10b). This significant increase

in correlation in the elastic regime is responsible for the majority of the 21% decrease in total L2-norm error (Fig. 8) observed between the Challenge-submission and Modification 1 models. Looking specifically at models that superpose the initial strain field (Modifications 1 and 2) compared to models that initialize an eigenstrain field (Modifications 3a, 3b, 4a, and 4b), there are some interesting trends to highlight. In the elastic regime, the strain superposition models have higher R^2 values than the eigenstrain models (Fig. 10b versus Fig. 10c), leading to the strain superposition models performing the best overall in the elastic regime (Fig. 8). This is because, in the elastic regime, superposing a set of elastic strains from experiment is generally considered valid and is a more explicit way of incorporating initial elastic strains than the eigenstrain approach. However, as more load is applied and plastic strain accumulates, the method of superposition breaks down, and the eigenstrain models begin to outperform the superposition models. Once the plastic regime is reached, the eigenstrain models have a lower L2-norm error and higher R^2 values than all other models in the plastic regime (Figs. 8 and 10c). The eigenstrain models perform best in this regime because the initial elastic strain field is inherently incorporated into the constitutive equations, allowing for stress equilibrium, strain compatibility, and grain rotation to be modeled more comprehensively. Interestingly, the eigenstrain models mainly improve the R^2 values of the axial strain (yy) component compared to the strain superposition models (Fig. 10c versus Fig. 10b). Compared to the spherical-grain assumption models (Modifications 3a and 3b), the ellipsoidal-grain shape assumption models (Modification 4a and 4b) have lower L2-norm errors (Fig. 8) as the equilibrated elastic strain fields have a stronger correlation to the initial elastic strain field (e.g., the 5.9% increase in average R^2 value in Table 4). Finally, when the correctional matrix is included in the spherical-grain Eshelby approximation (Modification 3b), the model predictions improve slightly over the uncorrected version (Modification 3a), and in the case of the ellipsoidal-grain Eshelby approximation (Modification 4b), the correctional matrix does not improve the predictions over the uncorrected version (Modification 4a). Additionally, all eigenstrain models perform almost identically to one another in the plastic regime. This is because, regardless of what the initial state of each grain is, the effective yield strength of each grain remains the same and thus the grain-averaged elastic strain tensors of each model effectively converge once each grain reaches plasticity.

Takeaways for Blind Micromechanical Predictions

We offer several key takeaways based on our experience participating in the AFRL AM Modeling Challenge and performing extensive post-Challenge analysis. First, the

EVPPFFT method is well equipped at handling micromechanical predictions given a 3D microstructure image. The EVPPFFT code can produce predictions below the ff-HEDM strain resolution in the elastic regime with straightforward input from a voxelized microstructure image. It was also found that improving the macroscopic stress–strain fit reduced the model bias in the axial strain components. Incorporating the initial elastic strain field was also found to be crucial for improving micromechanical predictions. The best method for this was found to be initializing an eigenstrain field using an ellipsoidal-grain Eshelby approximation. This method is relatively simple to implement and is a direct improvement over a spherical-grain Eshelby approximation, as it improves model predictions and requires no empirical correctional term.

If blind micromechanical model predictions akin to Challenge Problem 4 in the AFRL AM Modeling Challenge Series were to be made in the future using the EVPPFFT modeling method, the following steps would be performed. First, the given microstructure image would be modified as little as possible while still retaining the necessary EVPPFFT model requirements (e.g., buffer zone and, if needed, the 2ⁿ dimension requirement). If the residual initial elastic strain field is known (even for just a small subset of grains), an eigenstrain field would be calculated using an ellipsoidal-grain Eshelby approximation. Additionally, the mean initial elastic strain (if it exists) would be removed from the eigenstrain field calculations to nullify the net elastic strain at the initial state. The constitutive model parameters would then be optimized to minimize the total discrepancy between the experimental and simulated macroscopic stress–strain curves, *especially* at stress states of interest. Based on the presented results, taking these steps can substantially improve model performance and be easily verified.

Opportunities for Future Investigation

There are opportunities for potential improvements to the methods presented in this work, particularly in terms of the eigenstrain field calculations. The Eshelby approximation presented in this work assumes full isotropy; however, this assumption could be improved by using elastic properties calculated from the neighborhood of a respective grain. Coupled with this, Eshelby's tensor could be calculated using an anisotropic inclusion solution (e.g., Chapter 3 in Ref. [34]). These two methods are, however, much more complex to incorporate than the Eshelby approximation presented here. Pokharel and Lebensohn [21] previously proposed using an optimization-based approach to iteratively improve the eigenstrain field; however, this approach remains untested.

Beyond simply improving the methods presented here, there are several model additions that could be made. Given the constant decrease in model performance with increasing

plastic strain, improving plasticity modeling efforts is necessary. Numerous methods have been proposed to account for grain-boundary strengthening effects (an inherent plastic effect) within the EVPPFFT modeling method, ranging from dislocation-based models [41] to scaling the initial CRSS as a function of slip-directed distance to grain boundaries [42]. The EVPPFFT model used in this work does not explicitly consider any grain-size effects, and plasticity modeling improvements such as these could potentially resolve the axial-strain bias discussed previously. Precipitate data were also not considered in this work. Since the microstructure consisted of approximately 1.2% precipitate phase by volume-fraction, it is likely that these very small precipitate particles could have a considerable effect on the micro- and macroscopic response of the material. This precipitate phase could potentially be added through DREAM.3D [19] filters or other methods to more explicitly represent the multiphase microstructure, at the expense of increased computational cost due to a (likely) higher resolution simulation domain.

Conclusions

An EVPPFFT modeling approach was used to make blind predictions of micromechanical response for an experimentally characterized microstructure of additively manufactured IN625 in the context of Challenge Problem 4 in the AFRL AM Modeling Challenge series. The data provided to Challenge participants by AFRL included a 3D microstructural image (voxelized data set) depicting crystal orientations; a macroscopic engineering stress–strain curve corresponding to the aforementioned microstructure, with six specific stress states (S1–S6) indicated, at which far-field high-energy X-ray diffraction microscopy (ff-HEDM) measurements were collected; and grain-averaged elastic strains in each of the 28 Challenge grains at the initial state (S0). Participants were asked to predict the grain-averaged elastic strain tensor in each of the 28 Challenge grains at stress states S1 through S6. The Challenge-submission model reported here received the Top Performer Award for the lowest total L2-norm error (the grading metric calculated through comparison to experimental results) of all submissions. As a result of participating in the Challenge, the EVPPFFT formulation has been extended to simulate an arbitrary number of concatenated loading processes, enabling simulation of successive loading and unloading steps. After the Challenge—but without using any additional information—we investigated the impact of six model modifications on the predictive performance relative to the Challenge-submission model. From the results presented, the following conclusions are drawn:

1. Through post-Challenge investigation, we were able to substantially lower the total L2-norm error—by over

25% in the best model compared to our Challenge-submission model—using no additional information beyond what was provided to participants for the blind predictions.

2. Incorporating the initial residual strain field is crucial for improving prediction accuracy of *localized* micromechanical response. Models that incorporated the initial elastic strain field through any of the methods investigated herein reduced the total L2-norm error by at least 20% compared to the Challenge-submission model (in which initial strains were ignored), with the majority of this improvement occurring in the elastic regime. Leveraging residual strain data for even a small subset of grains (28 out of 29,663 grains in the case of the Challenge specimen) proved to be valuable in improving the overall accuracy of predictions.
3. Accounting for the initial residual strain field through the use of eigenstrains resulted in a significant improvement in predictive performance (based on overall L2-norm error) versus simply adding the initial elastic strains from experiment through superposition. While the superposition approach resulted in better performance metrics than the eigenstrain approach in the elastic regime (S1–S3), the latter outperformed the former in the plastic regime (S4–S6), accounting for the overall improvement in L2-norm error. The relative improvement of the eigenstrain models with increasing stress state is attributed to the fact that, unlike the simple superposition approach, the eigenstrain approach guarantees that the initial elastic strain field is inherently incorporated into the constitutive equations, allowing for stress equilibrium, strain compatibility, and grain rotation to be modeled more completely.
4. For the first time with respect to EVPFFT modeling, we report an ellipsoidal grain-shape assumption used in the Eshelby approximation to calculate an initial eigenstrain field. Using the parameters of a best-fit ellipsoid for each grain resulted in an equilibrated elastic strain field that more accurately represented the initial elastic strain field from experiment (i.e., an average R^2 increase of 5.9%) when compared to the eigenstrain field calculated based on a spherical grain-shape assumption. This more accurate representation of grain shape resulted in an improvement in model prediction compared to the spherical grain-shape assumption used previously.

Based on the lessons learned from the post-Challenge investigation, we offer a step-by-step procedure for using EVPFFT modeling to predict micromechanical response given a 3D microstructural image and known initial elastic strains (e.g., from ff-HEDM) for an incomplete set of grains in the microstructure. The findings presented herein have important implications for micromechanical modeling of

both conventionally manufactured and additively manufactured metals.

Appendix

Appendix A. Global and Local Model Convergence Study

During the post-Challenge analysis, a convergence study was completed to determine the optimal image resolution (voxel size) with respect to global and local error. The global error was calculated using the mean squared error (MSE) method given in Eq. (16), and the local error was calculated using the Challenge grading metric described in Eq. (1). The model inputs from Sect. 3.3.3 were used for the convergence study, aside from microstructure image resolution changes. For the purposes of the convergence study, a beta version of MASSIF with concatenated loading processes implemented was used. Utilizing MASSIF thus allowed for more data points (i.e., geometries that do not satisfy the 2ⁿ requirement) to be included in the convergence study than if the serial EVPFFT code were used. The local and global errors were calculated for seven different resolutions of the cuboidal voxel microstructure discussed in Sect. 3.3.2. The local and global error was additionally calculated for the original microstructure resolution provided for the Challenge (roughly 33 million voxels), i.e., a microstructure with no geometry modifications. Figure 12 shows the global and local error data for these eight microstructure resolutions.

From Fig. 12, the global error reached convergence before the local error. The global error reached convergence at about 1 million voxels or an average of about three voxels per grain (not shown in the plot), while the local error reached convergence at about 2.1 million voxels or an average of about 200 voxels per Challenge grain. Based on these results, the microstructure resolution used in all models presented herein did not have any significant effect on the model predictions.

Appendix B. Eigenstrain Calculations for Ellipsoidal Grains

The following calculations show the process of calculating the constant eigenstrain tensor using the dimensions of the best-fit ellipsoid of an individual grain. These calculations are implemented in DREAM.3D as the “Compute Eigenstrains by Feature (Grain/Inclusion)” filter as of version 6.5.151. The DREAM.3D filter does not have an option to subtract the mean initial elastic strain tensor as

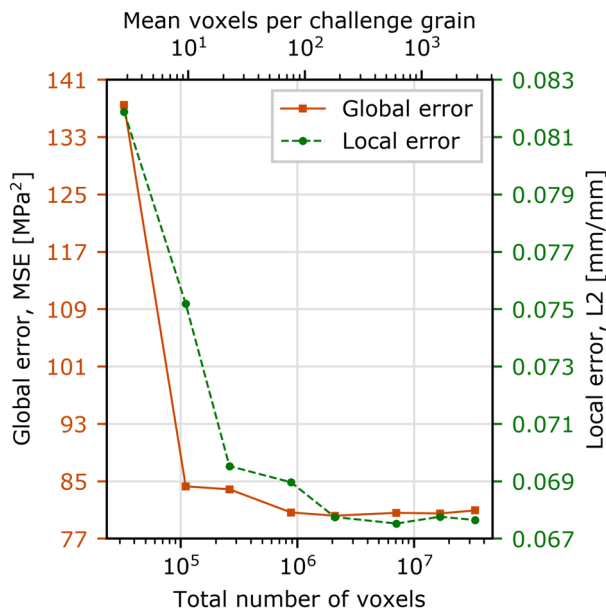


Fig. 12 Convergence plot showing the total number of voxels versus global error (MSE) and local error (L2). The global error was calculated with Eq. (16), and the local error was calculated with Eq. (1). The top horizontal axis indicates the mean number of voxels comprising each Challenge grain. The two lowest resolution microstructures entirely removed one or more Challenge grains, so an average error from the remaining grains was used to fill those values

in Eq. (18), so that must be performed manually if desired. The first calculation is to change the basis of the elastic strain tensor into the best-fit ellipsoid (local) reference frame, i.e.,

$$\epsilon_{kl}^{e'} = Q_{ki} Q_{lj} \epsilon_{ij}^e, \tag{22}$$

where $\epsilon_{kl}^{e'}$ is the elastic strain tensor in the local reference frame and Q_{ki} is the orientation matrix corresponding to the orientation of the best-fit ellipsoid reference frame. The prime (') superscript indicates a tensor in the local reference frame and the absence of such indicates a tensor in the global reference frame. Next, the fourth-rank Eshelby tensor is calculated via Eshelby's solution [37] for isotropic ellipsoidal inclusions using Eqns. 11.16–11.19 given by Mura [34], where Eshelby's tensor, S_{ijkl} , is a function of the ellipsoid semi-axis lengths, $a \geq b \geq c$, and Poisson's ratio, ν . Edge cases where the grain shape is a sphere or spheroid are handled using Eqns. 11.21, 11.28, and 11.29 given by Mura [34]. Within Eshelby's solution, there are two elliptic integrals that are numerically integrated using 32-point Gaussian quadrature (arbitrarily chosen as execution time is negligible). Once Eshelby's tensor is calculated, the uniform eigenstrain tensor is calculated in the local reference frame as follows:

$$\epsilon_{ij}^{*'} = (S_{ijkl} - I_{ijkl})^{-1} \epsilon_{kl}^e, \tag{23}$$

where $\epsilon_{ij}^{*'}$ is the eigenstrain tensor in the local reference frame. This fourth-rank tensor inversion is performed on a flattened 9×9 matrix and then rebuilt into a fourth-rank tensor. The final calculation is to transform the eigenstrain tensor back into the global reference frame to complete the eigenstrain calculations as follows:

$$\epsilon_{kl}^* = Q_{ik} Q_{jl} \epsilon_{ij}^{*'}, \tag{24}$$

where ϵ_{kl}^* is the final eigenstrain tensor. The correctional matrix can then be applied through Eq. 20, if desired. These calculations are then repeated for every grain in the microstructure, which is 29,663 grains in the case of the Challenge microstructure.

Supplementary Information The online version contains supplementary material available at <https://doi.org/10.1007/s40192-021-00211-w>.

Acknowledgements CKC acknowledges support provided by the US Department of Energy Office of Nuclear Energy's Nuclear Energy University Program (NEUP) under Grant No. DE-NE0008799. ADS and ADR acknowledge support provided by the Department of Defense Office of Economic Adjustment under award no. ST1605-19-03. RAL acknowledges support from DOE-DOD Joint Munitions Program. The support and resources from the Center for High Performance Computing at the University of Utah are gratefully acknowledged.

Declarations

Conflict of interest On behalf of all authors, the corresponding author states that there is no conflict of interest.

References

1. King WE, Anderson AT, Ferencz RM, Hodge NE, Kamath C, Khairallah SA, Rubenchik AM (2015) Laser powder bed fusion additive manufacturing of metals; physics, computational, and materials challenges. *Appl Phys Rev* 2(4):041304
2. Francois MM, Sun A, King WE, Henson NJ, Tournet D, Bronkhorst CA, Carlson NN, Newman CK, Haut TS, Bakosi J et al Modeling of additive manufacturing processes for metals: challenges and opportunities. *Current Opin Solid State Mater Sci* 21 (LA-UR-16-24513; SAND-2017-6832J)
3. Kouraytem N, Li X, Tan W, Kappes B, Spear A Modeling process-structure-property relationships in metal additive manufacturing: a review on physics-driven versus data-driven approaches. *J Phys Mater* 4:032002
4. Gatsos T, Elsayed KA, Zhai Y, Lados DA (2020) Review on computational modeling of process-microstructure-property relationships in metal additive manufacturing. *JOM* 72(1):403–419
5. Boyce BL, Kramer SL, Fang HE, Cordova TE, Neilsen MK, Dion K, Kaczmarowski AK, Karasz E, Xue L, Gross AJ et al (2014) The sandia fracture challenge: blind round robin predictions of ductile tearing. *Int J Fract* 186(1–2):5–68
6. Boyce B, Kramer S, Bosiljevac T, Corona E, Moore J, Elkhodary K, Simha C, Williams B, Cerrone A, Nonn A et al (2016) The

- second Sandia fracture challenge: predictions of ductile failure under quasi-static and moderate-rate dynamic loading. *Int J Fract* 198(1):5–100
7. Kramer SL, Jones A, Mostafa A, Ravaji B, Tancogne-Dejean T, Roth CC, Bandpay MG, Pack K, Foster JT, Behzadinasab M et al (2019) The third Sandia fracture challenge: predictions of ductile fracture in additively manufactured metal. *Int J Fract* 218(1):5–61
 8. Levine L, Lane B, Heigel J, Migler K, Stoudt M, Phan T, Ricker R, Strantza M, Hill M, Zhang F, Seppala J, Garboczi E, Bain E, Cole D, Allen A, Fox J, Campbell C, (2018) Outcomes and conclusions from the AM-bench measurements, challenge problems, modeling submissions, and conference. *Integr Mater Manuf Innov*. <https://doi.org/10.1007/s40192-019-00164-1>
 9. Suter R, Hennessy D, Xiao C, Lienert U (2006) Forward modeling method for microstructure reconstruction using x-ray diffraction microscopy: single-crystal verification. *Rev Sci Instrum* 77(12):123905
 10. Bernier JV, Barton NR, Lienert U, Miller MP (2011) Far-field high-energy diffraction microscopy: a tool for intergranular orientation and strain analysis. *J Strain Anal Eng Des* 46(7):527–547
 11. Lienert U, Li S, Hefferan C, Lind J, Suter R, Bernier J, Barton N, Brandes M, Mills M, Miller M et al (2011) High-energy diffraction microscopy at the advanced photon source. *JOM* 63(7):70–77
 12. Pokharel R (2018) Overview of high-energy x-ray diffraction microscopy (HEDM) for mesoscale material characterization in three-dimensions, In: *Materials Discovery and Design*, Springer, pp. 167–201
 13. Kocks UF, Tomé C, Wenk H-R (1998) *Texture and anisotropy*. Cambridge University Press, Cambridge, UK
 14. Choi YS, Groeber MA, Shade PA, Turner TJ, Schuren JC, Dimiduk DM, Uchic MD, Rollett AD (2014) Crystal plasticity finite element method simulations for a polycrystalline Ni micro-specimen deformed in tension. *Metall Mater Trans A* 45(13):6352–6359
 15. Pokharel R, Lind J, Kanjarla A, Lebensohn R, Li S, Kenesei P, Suter R, Rollett A (2014) Polycrystal plasticity: comparison between grain scale observations of deformation and simulations. *Annu Rev Condens Mat Phys* 5:317–346
 16. Shade PA, Blank B, Schuren JC, Turner TJ, Kenesei P, Goetze K, Suter RM, Bernier JV, Li SF, Lind J, Lienert U, Almer J (2015) A rotational and axial motion system load frame insert for in situ high energy x-ray studies. *Rev Sci Instrum* 86(9):093902. <https://doi.org/10.1063/1.4927855>
 17. Menasche DB, Musinski WD, Obstalecki M, Shah MN, Donegan SP, Bernier JV, Kenesei P, Park J-S, Shade PA AFRL additive manufacturing modeling series: challenge 4, in situ mechanical test of an IN625 sample with concurrent high-energy diffraction microscopy characterization
 18. Chapman MG, Shah MN, Donegan SP, Scott JM, Shade PA, Menasche D, Uchic MD AFRL additive manufacturing modeling series: challenge 4, 3d reconstruction of an IN625 high-energy diffraction microscopy sample using multi-modal serial sectioning
 19. Groeber M, Jackson M (2014) Dream.3d: a digital representation environment for the analysis of microstructure in 3d. *Integr Mater Manuf Innov* 3:5. <https://doi.org/10.1186/2193-9772-3-5>
 20. Lebensohn RA, Rollett AD (2020) Spectral methods for full-field micromechanical modelling of polycrystalline materials. *Comput Mater Sci* 173:109336. <https://doi.org/10.1016/j.commatsci.2019.109336>
 21. Pokharel R, Lebensohn RA (2017) Instantiation of crystal plasticity simulations for micromechanical modelling with direct input from microstructural data collected at light sources. *Scripta Mater* 132:73–77. <https://doi.org/10.1016/j.scriptamat.2017.01.025>
 22. Lebensohn RA, Kanjarla AK, Eisenlohr P (2012) An elastoviscoplastic formulation based on fast Fourier transforms for the prediction of micromechanical fields in polycrystalline materials. *Int J Plasticity* 32–33:59–69. <https://doi.org/10.1016/j.ijplas.2011.12.005>
 23. Moulinec H, Suquet P (1998) A numerical method for computing the overall response of nonlinear composites with complex microstructure. *Comput Methods Appl Mech Eng* 157(1):69–94. [https://doi.org/10.1016/S0045-7825\(97\)00218-1](https://doi.org/10.1016/S0045-7825(97)00218-1)
 24. Lebensohn RA (2001) N-site modeling of a 3d viscoplastic polycrystal using fast Fourier transform. *Acta Mater* 49(14):2723–2737. [https://doi.org/10.1016/S1359-6454\(01\)00172-0](https://doi.org/10.1016/S1359-6454(01)00172-0)
 25. Michel JC, Moulinec H, Suquet P (2000) A computational method based on augmented lagrangians and fast Fourier transforms for composites with high contrast. *Comput Model Eng Sci* 1(2):79–88. <https://doi.org/10.3970/cmcs.2000.001.239>
 26. Lebensohn RA, Brenner R, Castelnau O, Rollett AD (2008) Orientation image-based micromechanical modelling of subgrain texture evolution in polycrystalline copper. *Acta Mater* 56(15):3914–3926. <https://doi.org/10.1016/j.actamat.2008.04.016>
 27. Frigo M, Johnson SG (2005) The design and implementation of FFTW3. *Proceedings of the IEEE* 93 (2) 216–231, special issue on “Program Generation, Optimization, and Platform Adaptation”
 28. The HDF Group, Hierarchical data format version 5 (2021). <http://www.hdfgroup.org/HDF5>
 29. Wang Z, Stoica AD, Ma D, Beese AM (2016) Diffraction and single-crystal elastic constants of inconel 625 at room and elevated temperatures determined by neutron diffraction. *Mater Sci Eng A* 674:406–412. <https://doi.org/10.1016/j.msea.2016.08.010>
 30. Michel JC, Moulinec H, Suquet P (2001) A computational scheme for linear and non-linear composites with arbitrary phase contrast. *Int J Numer Meth Eng* 52(1–2):139–160. <https://doi.org/10.1002/nme.275>
 31. Powell MJD (1964) An efficient method for finding the minimum of a function of several variables without calculating derivatives. *Comput J* 7(2):155–162. <https://doi.org/10.1093/comjnl/7.2.155>
 32. Virtanen P, Gommers R, Oliphant TE, Haberland M, Reddy T, Cournapeau D, Burovski E, Peterson P, Weckesser W, Bright J, van der Walt SJ, Brett M, Wilson J, Millman KJ, Mayorov N, Nelson ARJ, Jones E, Kern R, Larson E, Carey CJ, Polat İ, Feng Y, Moore EW, VanderPlas J, Laxalde D, Perktold J, Cimrman R, Henriksen I, Quintero EA, Harris CR, Archibald AM, Ribeiro AH, Pedregosa F, van Mulbregt P (2020) SciPy 1.0 contributors, SciPy 1.0: fundamental algorithms for scientific computing in python 17:261–272. <https://doi.org/10.1038/s41592-019-0686-2>
 33. Herrera-Solaz V, LLorca J, Dogan E, Karaman I, Segurado J (2014) An inverse optimization strategy to determine single crystal mechanical behavior from polycrystal tests: Application to AZ31 mg alloy. *Int J Plasticity* 57:1–15. <https://doi.org/10.1016/j.ijplas.2014.02.001>
 34. Mura T (1987) *Micromechanics of defects in solids*, 2nd edn. Martinus-Nijhoff, Dordrecht
 35. Hershey A (1954) The elasticity of an isotropic aggregate of anisotropic cubic crystals. *J Appl Mech Trans ASME* 21(3):236–240
 36. Tari V, Lebensohn RA, Pokharel R, Turner TJ, Shade PA, Bernier JV, Rollett AD (2018) Validation of micro-mechanical fft-based simulations using high energy diffraction microscopy on Ti-7Al. *Acta Mater* 154:273–283. <https://doi.org/10.1016/j.actamat.2018.05.036>
 37. Eshelby J (1957) The determination of the elastic field of an ellipsoidal inclusion, and related problems. *Proc R Soc Lond A* 241:376–396
 38. Groeber M, Ghosh S, Uchic MD, Dimiduk DM (2008) A framework for automated analysis and simulation of 3d polycrystalline microstructures: part I: statistical characterization. *Acta Mater* 56(6):1257–1273. <https://doi.org/10.1016/j.actamat.2007.11.041>
 39. Bernier JV, Suter RM, Rollett AD, Almer J (2020) High energy diffraction microscopy in materials science. *Annu*

- Rev Mater Res 50:395–436. <https://doi.org/10.1146/annurev-matsci-070616-124125>
40. Tukey JW (1949) Comparing individual means in the analysis of variance. *Biometrics* 5(2):99–114
 41. Berbenni S, Taupin V, Lebensohn RA (2020) A fast Fourier transform-based mesoscale field dislocation mechanics study of grain size effects and reversible plasticity in polycrystals. *J Mech Phys Solids* 135:103808. <https://doi.org/10.1016/j.jmps.2019.103808>
 42. Herriott C, Li X, Kourayem N, Tari V, Tan W, Anglin B, Rollett AD, Spear AD (2019) A multi-scale, multi-physics modeling

framework to predict spatial variation of properties in additive-manufactured metals. *Model Simul Mater Sci Eng* 27(2):025009. <https://doi.org/10.1088/1361-651x/aaf753>

Publisher's Note Springer Nature remains neutral with regard to jurisdictional claims in published maps and institutional affiliations.